Comparison of dc and superconducting rf photoemission guns for high brightness high average current beam production

Ivan V. Bazarov, Allen Kim, Manu N. Lakshmanan, and Jared M. Maxson

Cornell Laboratory for Accelerator-based Sciences and Education, Cornell University, Ithaca, New York 14853, USA
(Received 8 April 2011; published 15 July 2011)

A comparison of the two most prominent electron sources of high average current high brightness electron beams, dc and superconducting rf photoemission guns, is carried out using a large-scale multivariate genetic optimizer interfaced with space charge simulation codes. The gun geometry for each case is varied concurrently with laser pulse shape and parameters of the downstream beam line elements of the photoinjector to obtain minimum emittance as a function of bunch charge. Realistic constraints are imposed on maximum field values for the two gun types. The superconducting rf and dc gun emittances and beam envelopes are compared for various values of photocathode thermal emittance. The performance of the two systems is found to be largely comparable for up to 154 pC per bunch at 1.3 GHz or 200 mA provided low intrinsic emittance photocathodes can be employed.

I. INTRODUCTION

To realize the fullest potential in a range of applications, energy recovery linacs (ERLs) require high brightness electron beams that are currently beyond the state of the art. In addition to very low beam emittances (≤ 1 μm rms normalized), these sources need to provide high average currents (~ 100 mA). Photoemission guns, whether utilizing a dc high voltage gap or an rf resonant cavity, have become the technology of choice and remain a key component in photoinjectors. Several efforts are underway in the accelerator community to advance the electron source technology towards generating higher average current and lower emittance beams.

Normal conducting rf guns have performed well in pulsed applications, e.g., see [1]. Continuous-wave (cw) operation tends to be limited to a lower frequency range (below a GHz) [2] and the problems of Ohmic wall losses appear prohibitive for the L band frequency range. dc and superconducting rf (SRF) guns are free of this limitation, which allows the excellent vacuum necessary for high quantum efficiency photocathodes.

Both technologies are actively pursued at the moment at a number of laboratories; for an overview refer to [3,4]. It is important to understand the main limitations in both cases. dc guns are mainly limited by field emission, whereas SRF guns should allow operation with much higher fields. However, the introduction of a photocathode transport system with load-lock into a clean SRF gun environment without unwanted field emission remains a challenge. The implications of beam dynamics are very different for the

two gun types as well. Higher accelerating gradient is of advantage in SRF guns for space charge dominated beams. dc guns, on the other hand, are free of time-dependent forces, which allows for small aberrations, as well as longer bunches to reduce the effect of space charge forces.

In this paper we present a comparison of the two gun types for the production of low emittance high average current beams from the point of beam dynamics and emittance performance. In simulations, each gun is followed by a short 1.3-GHz accelerating section (existing Cornell ERL injector cryomodule) that takes the beam energy to 10–12 MeV where the effect of space charge forces on beam emittance is considerably reduced. We use a genetic multiobjective algorithm [5], which proved to be a powerful tool in the accelerator design. Additionally, we implemented flexible (adjustable) gun geometries for both dc and SRF guns to allow for lowest emittance production. In each of the two gun types, constraints are imposed in order to obtain a realistic assessment of their performance and its implications on beam brightness. Additionally, we investigate the effects of the intrinsic photocathode emittance, the laser shape, and various emittance diluting mechanisms present in the system.

While both technologies will continue to be developed, this study presents a self-consistent comparison from the beam performance point of view. It is shown that either technology is capable of generating ultralow emittance beams necessary for the next generation high current and brightness accelerators. The results indicate that successfully implemented SRF guns should allow superior performance for photocathodes with high intrinsic emittance, whereas the two technologies are largely equivalent in emittance when very low thermal emittance photocathodes are utilized [6].

In what follows, we introduce our numerical method and explain the variable geometry of the guns as well as the

photoinjector beam line used to compare the two technologies. Following the presentation of the main results, we investigate various emittance limiting and degrading mechanisms in both dc and SRF gun-based photoinjectors.

II. NUMERICAL METHOD

For the purpose of this study, we explore average currents delivered out of each gun of up to 200 mA, or 154 pC/bunch at 1.3 GHz beam repetition rate, with pulses of 0.9 mm rms bunch length (3 ps) at the end of the photoinjector for either gun choice. Beam dynamics in photoinjectors at such charge and bunch duration is dominated by space charge phenomena, and experimentally benchmarked codes are essential to understand beam performance implications. There has been an effort in the accelerator community to benchmark the space charge codes and overall good agreement between beam measurements and simulations exists (for example, see [7]). We implemented the genetic algorithm optimizer to use two different space charge codes: GPT (3D) [8] and ASTRA (2D radially symmetric) [9], which demonstrate excellent agreement between each other and the experimental measurements. Because of the axial symmetry of all the beam elements in the studied photoinjector and in the interest of efficiency, the results presented in this paper were obtained with ASTRA.

A. Optimizer structure

Our previous work [10] introduced a genetic multiobjective optimization for the photoinjector design. The main advantage of this method is that optimal fronts are obtained, which show the tradeoffs and dependencies in various parameters. This is to be contrasted with a single point conventional design approach (e.g., a single bunch charge). Detailed space charge simulations are computationally expensive and, as previously, a computer cluster is used in these studies.

An important addition to the optimizer is its newly implemented ability to vary the field maps of individual accelerator elements. Precomputed field maps from a parametrized geometry of an element (dc or SRF gun in this case) are combined in such a way as to allow the generation of new field maps corresponding to new shapes. This process is controlled by the optimizer in minimizing the figures of merit.

Our optimization package is a set of codes that modularizes the optimization process. The optimization process has two main components: the selector and the variator [11,12]. The algorithm begins with the selector forming a trial set of decision variable solutions that the variator then uses in either ASTRA or GPT simulations of the beam line, the results of which are returned to the selector. Then the selector chooses the "fittest" solutions from the set, based on several (typically two) criteria, known as "objectives."

To form a new trial set for the next generation of solutions, the selector applies two operators to the selected fittest solutions of the previous generation: (1) "crossing," or "mating," of two or more solutions; and (2) slightly perturbing ("mutating") each solution to form a new solution ("offspring"). The process is then repeated with the newly formed set of offspring solutions and continues for a number of generations, effectively exploring the decision variable space for the best solutions. In the process, the selector also subjects the solutions to a set of constraints to ensure physically realistic scenarios. Finally, the algorithm presents a set of optimal solutions as the optimal front. In our study, the objectives are minimum beam emittance and maximum bunch charge, constrained so that the current in the injector does not exceed 200 mA, the final bunch duration to be less than 3 ps rms, and that the fields in dc and SRF guns remain below the physical maxima (detailed below). We expect the minimum emittance solutions to be those with low bunch charge, and thus the inclusion of bunch charge as an objective effectively serves to scan the emittance over the entire range of bunch charges.

The optimizer as a whole will seek to evaluate different solutions with various beam parameters, and more challengingly, solutions with different gun geometries. Field maps for a requested gun geometry could be calculated during optimization; however, we have found it more computationally efficient to calculate field maps for a discrete set of gun geometries prior to the optimization run. These field maps, calculated and postprocessed with POISSON-SUPERFISH [13], are tabulated based on a number of geometry parameters and figures of merit (angles, electric field at the photocathode, peak fields, etc.). The optimizer selects from a continuous space of these geometry parameters, wherein the requested map and its figures of merit are interpolated on the multidimensional geometry parameter space.

A powerful addition to the optimizer has been the inclusion of constraints that are any algebraic relationship of the above geometry parameters, figures of merit, or simulation outputs. For instance, this has enabled the implementation of the empirical voltage breakdown condition, which is a power law function relating the dc voltage, and dc gun cathode-anode separation. Furthermore, this capability allows mid-optimization calculation of various functions that depend on both geometry and field map figures of merit.

We have taken the following steps to ensure adequate convergence of each optimization given the finite duration of each run. The number of generations (typically 1500 generations with 75 member population per generation) was chosen such as to make the smooth trend of the optimal front visible well above the statistical noise floor. Furthermore, the optimization runs have been repeated for initial populations with different random seeds to ensure the behavior of the solutions (overall gun geometry and final emittance) remained consistent and did not depend on a particular random seed chosen.

B. dc gun geometry parameters

The dc gun geometry parameters that are varied are the Pierce electrode angle, the cathode-anode gap, and the photocathode recess, as shown in Fig. 1. The cathode recess has an effect of fine-tuning electrostatic focusing at the photocathode. At the end, however, the recess was found to be a relatively unimportant parameter for the final injector performance. The gun voltage is also varied directly, being only limited by vacuum breakdown [Figs. 1(b) and 1(c) depict the highest allowable voltages].

In our optimizations, the gap was allowed to vary from 2–12 cm, the angle between 0–45°, and the recessed between 0–2 mm. There are a number of emittance trade-offs when varying gun geometry. An increased angle provides greater focusing, beneficial to counteract space charge, but also decreases the field at the photocathode surface. Decreasing the gap will strengthen the field at the photocathode surface, but will also increase the intrinsic effect of anode defocusing. The voltage and gap will be ultimately limited by the vacuum breakdown limit, to be discussed in Sec. II D.

C. SRF gun geometry parameters

We use a one-(or half-)cell SRF cavity design. While it might be beneficial to use multiple cells, our choice was motivated by both simplicity and input coupler considerations. The beam energy even after a one-cell SRF gun can approach 2 MeV in our optimizations, requiring 400 kW power coupled into 200 mA beam (the highest average current considered in this study). These power levels become problematic for input couplers at 1.3 GHz and a larger number of cells has been ruled out. For the very same reason, the energy boosting cavities in the Cornell ERL injector cryomodule design have only two-cell cavities at a more modest gradient, each equipped with twin input couplers capable of delivering ~120 kW rf power into the beam.

The 1.3 GHz SRF gun cavity geometry is shown in Fig. 2. The SRF gun has five varied parameters: the photocathode radius r_{cath}, the angle of the leftmost cavity wall α, and to a lesser extent the photocathode recess d, will affect the initial focusing, whereas the gap g and exit pipe radius r_{pipe} will determine the extent of the cavity field into the exit pipe. The equatorial cavity radius is used as the parameter for frequency tuning, which is iteratively performed for each set of geometry parameters. We have allowed the following parameter ranges: α is varied between 0–50°, g between 1.5–13.5 cm, d from 0–2.5 mm, $1/r_{cath}$ between 0–0.1 mm^{-1}, and r_{pipe} from 0.8–3.9 cm. Not all geometries within the scanned space can be tuned to 1.3 GHz or are even possible; however, the successfully
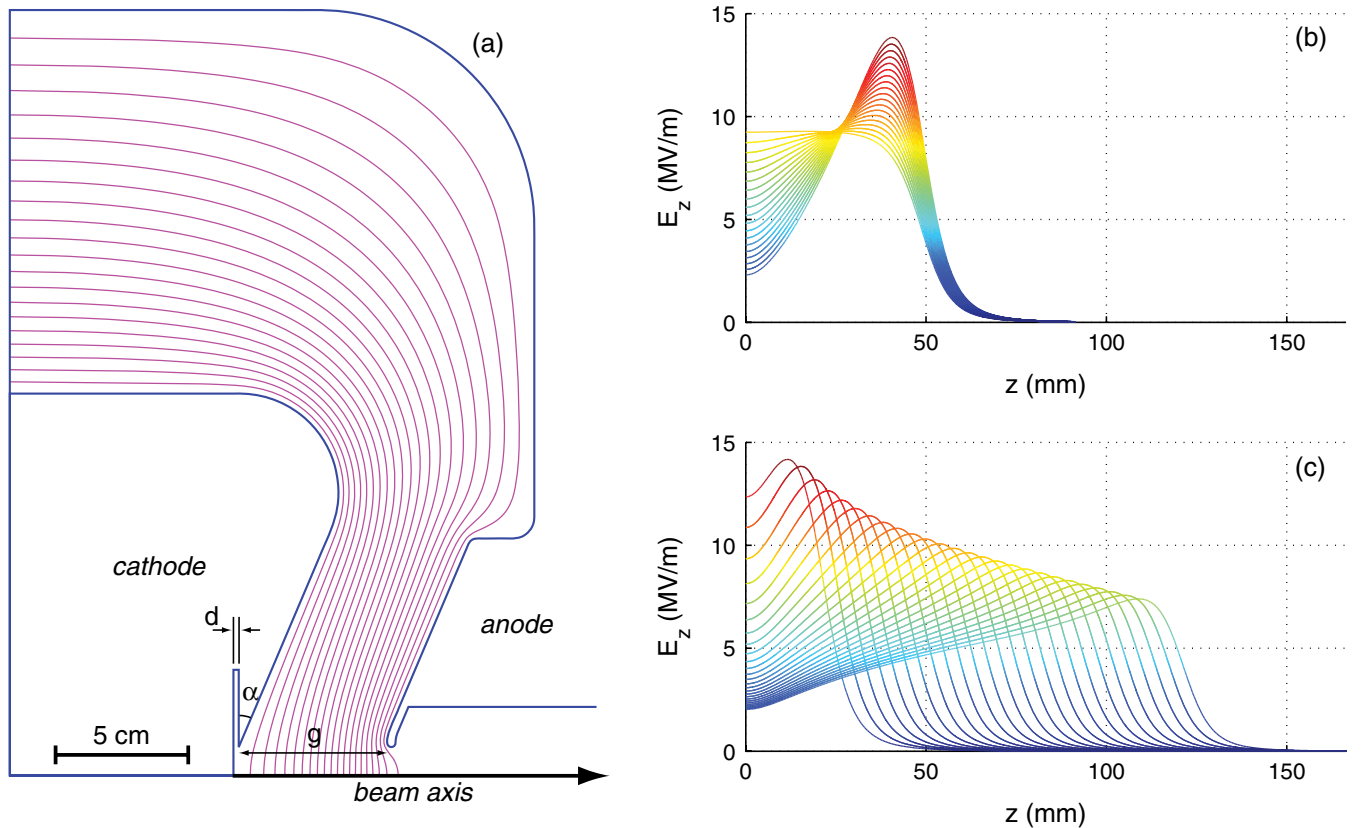

FIG. 1.   (a) The parametrized dc gun geometry: the electrode angle α, the cathode-anode gap g, and the photocathode recess d are the parameters varied by the optimizer. Equipotential lines are shown. (b) The effect of varying the angle α (from 0 to 45°) on the axial electric field for a fixed gap $g = 48$ mm. (c) The effect of varying the gap g (from 20 to 120 mm) for a fixed $\alpha = 23°$.
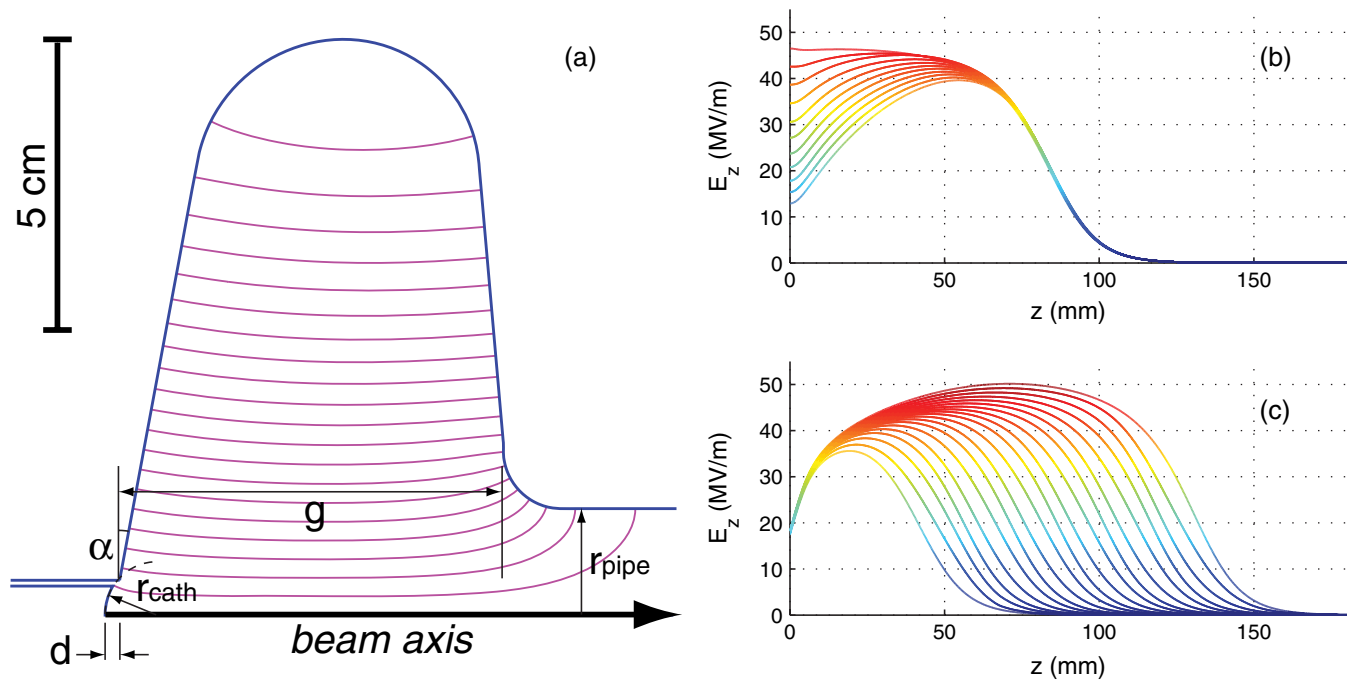
FIG. 2. (a) The parameters of the SRF cavity geometry, modeled after the 1.3 GHz TESLA design. The radius r_{cath} and recess d of the photocathode, the angle α of the leftmost cavity wall, the gap g between photocathode and exit pipe, and the exit pipe radius r_{pipe} are varied, with the equatorial cavity radius left as the free parameter for frequency tuning. Here, lines of constant azimuthal magnetic field are shown. (b) The effect of varying the angle α (from 0 to 25°) on the axial electric field for fixed $g = 75$ mm, $r_{pipe} = 1.83$ cm, $d = 0$, and $1/r_{cath} = 0$. (c) The effect of varying the gap g (from 15 to 105 mm) for fixed $\alpha = 10.5°$, $d = 1.67$ mm, $r_{cath} = 15$ mm, and $r_{pipe} = 1.83$ cm.

generated geometries were seen to form a connected set, as expected. In Figs. 2(b) and 2(c), the maximum surface electric and magnetic fields are constrained to be equal to the values found in the TESLA nine-cell cavity structure [14] at $E_{acc} = 25$ MV/m.

D. Vacuum breakdown and critical fields

It is essential to constrain maximum fields achievable in respective gun types for a meaningful comparison. For the case of the dc gun, a fundamental limitation is vacuum breakdown precipitated by field emission. In addition to the material choice, surface preparation as well as the area and the gap separating the electrodes play an important role. While ceramic puncture is the present limitation in raising gun voltage higher for many existing dc guns, technological solutions such as the use of segmented, shielded ceramic [15] may entirely mitigate the puncture problem. In this case, the emphasis is shifted towards the fields in the beam region of the cathode-anode gap. While the field emission current scaling is well known via the Fowler-Nordheim relations, field emission sites, often caused by inclusions within the electrode material, are highly stochastic in concentration, and cross-talk mechanisms between the anode and the cathode (e.g. x-ray generation, electron-induced gas desorption, etc.) make the onset of the field emission notoriously difficult to predict.

However, empirical data have been collected in [16] concerning vacuum breakdown voltage as a function of gap, which is plotted for our region of interest in Fig. 3. In the figure, s is the shortest distance between the cathode and the anode, approximately given by $s \approx g \cos(\alpha)$.
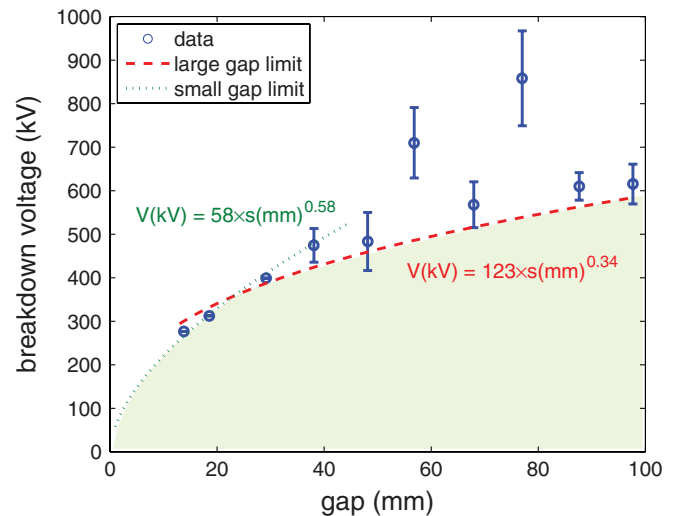

FIG. 3. Empirical data of voltage breakdown as a function of gap for planar electrodes, after [16], including fits used in constraining solutions. The filled area shows allowed values. Here, s is defined as the shortest distance between the cathode and anode.

The breakdown voltage is computed for each combination of the gun geometry parameters and if the gun voltage exceeds the breakdown voltage, that trial solution is invalidated.

SRF guns are also prone to field emission problems [4]. One important challenge is an introduction of the photocathode (via a load-lock) into the ultraclean SRF cavity environment. A number of SRF guns have displayed high levels of the field emission, which is especially significant when high quantum efficiency materials are present in the system. We use an optimistic criterion with fields being limited by the standard TESLA cavity parameters at $E_{\mathrm{acc}} = 25$ MV/m, which will undoubtedly be more difficult to achieve in an SRF photoemission gun. Both peak electric field E_{pk} and magnetic field H_{pk} at the niobium surface is calculated for each gun geometry. The following requirements are imposed during simulations $E_{\mathrm{pk}}/E_{\mathrm{acc}} \leq 2$ and $H_{\mathrm{pk}}/E_{\mathrm{acc}} \leq 4.26$ mT/(MV/m) [14]. We find that the majority of solutions within our parameter space were limited by the restriction on the surface electric field (< 50 MV/m).

One of the main purposes of the present work is to introduce the novel features of the optimizer suite. In order to reduce the computational load and to enhance clarity, we limited our design considerations to those most pertinent to the Cornell ERL project. Furthermore, we have not exhausted the geometry parameter space in either gun type. For instance, in the dc case, we have excluded the scanning of the overall electrode radius, nor do we consider the full geometry including stalk and ceramic regions. In the SRF case, we have chosen not to vary the cathode rod radius; however, we feel that the inclusion of the recess and the photocathode radius of curvature as parameters will scan over similar focusing fields. Future studies within the injector community using similar methodologies can and should highlight different parameters as required by a particular application.

III. OPTIMIZATION PARAMETERS

A. Beam line

Both the SRF and dc beam lines are modeled after the existing Cornell ERL injector, a schematic of which is shown in Fig. 4. The dc beam line has no modifications to the Cornell injector, which includes two emittance compensating solenoids with a normal conducting rf bunching cavity, followed by a 5-m long cryomodule with five two-cell 1.3 GHz SRF cavities, and then a drift section until the emittance measurement system at $z = 9.5$ m from the photocathode.

The buncher cavity is operated at zero crossing and is used to compress the electron bunches. This works very well due to the low energy out of the dc gun requiring only modest buncher fields. However, in the case of the SRF gun, owing to the higher gun energy, the buncher is of limited utility. Thus, it was completely eliminated, and the beam line for the SRF gun-based photoinjector has only one solenoid between the SRF gun and the energy boosting cryomodule. We have chosen a distance of 40 cm between the solenoid center and the gun photocathode to allow for sufficient magnetic field attenuation at the niobium structure.

Refer to Fig. 5 for an example of axial fields for both photoinjector types. Each magnet current, cavity phase, and amplitude are varied by the optimizer. All the beam line elements can adopt a range of values that have been demonstrated in the Cornell ERL photoinjector (e.g. the maximum electric field on axis in SRF two-cell cavities stays below 30 MV/m, while the rf buncher does not exceed ~2 MV/m).

B. Photocathode and laser shaping

Photocathode properties play an important role in production of high brightness electron beams. The mean transverse energy (MTE) associated with photoemitted electrons along with the cathode electric field set a limit to the highest beam brightness available from a photoinjector [17]. In terms of the laser rms spot size σ_{xy}, the intrinsic emittance (rms normalized) from the photocathode is given by

$$\epsilon_{nxy,\mathrm{th}} = \sigma_{xy}\sqrt{\frac{\mathrm{MTE}}{mc^2}}, \tag{1}$$

where mc^2 is the electron rest energy. Additionally, photoemission response time impacts the effective use of laser shaping. Several photocathode materials hold immediate promise. K_2CsSb has good quantum efficiency at a
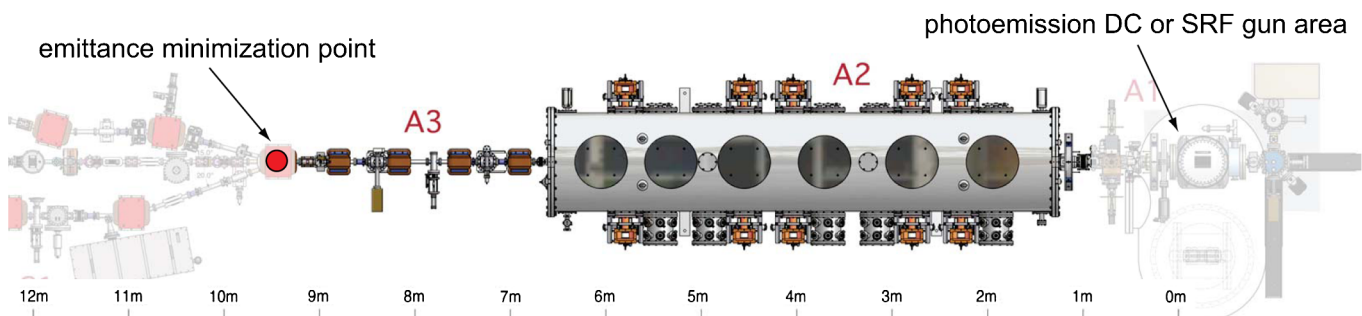

FIG. 4.   Injector layout modeled after Cornell ERL electron source. The beam direction is to the left.
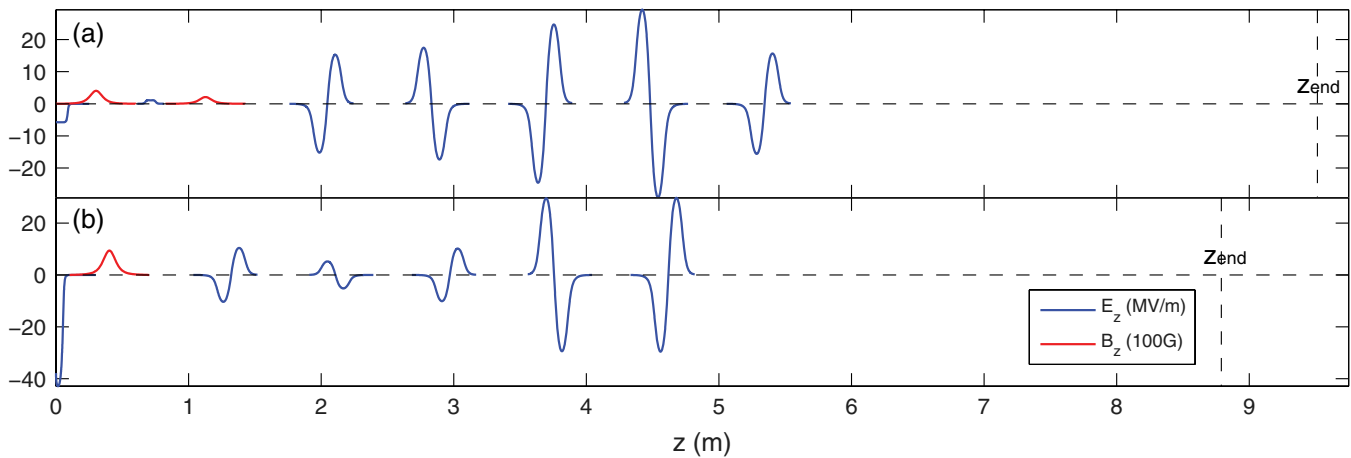
FIG. 5. Typical axial fields in the injector: (a) the dc and (b) the SRF gun based.

convenient laser wavelength (green) and additionally demonstrates good longevity for high average current applications. Its exact value for MTE is still under investigation. GaAs features very low MTE $= 0.12$ eV at 520 nm and a prompt [18] response (< 1 ps). In this study we use three values for MTE: 0.5, 0.12, and 0.025 eV, where 0.025 eV corresponds to the room temperature, and is the lowest value that has been measured for any photocathode to date [6,18].

To achieve very small emittances, it is essential to control space charge forces via laser shaping. For a dc beam, a transverse flattop distribution is ideal as it generates linear space charge forces that do not increase beam emittance. For beams in free space, a uniform density 3D ellipsoid gives a linear force in any direction. The conducting boundary condition at the photocathode surface changes this idealized picture. Additionally, the space charge forces can couple transverse and longitudinal motion. We have included several parameters to optimize the temporal
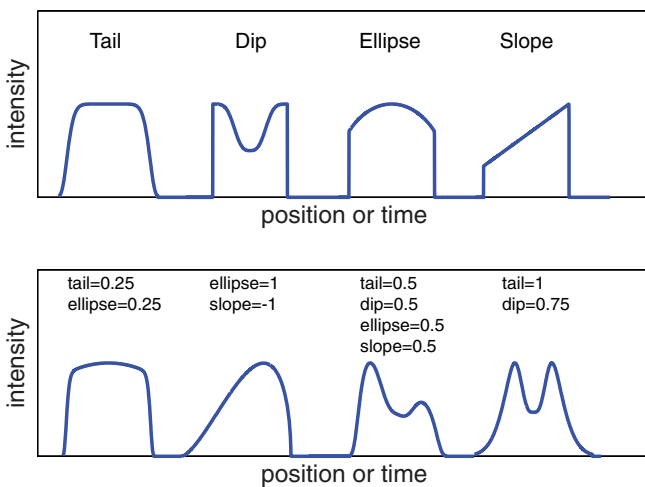

FIG. 6. Above: Archetypal laser pulse shapes, variably superimposed to form the requested laser pulse shape. Below: Sample pulse shapes including their superposition parameters.

profile of the laser pulse by allowing a wide range of pulse templates to explore effective laser shapes from the electron beam dynamics point of view. These pulse templates are shown in Fig. 6. We have allowed the laser pulse duration to vary between 0 and 30 ps. The longer bunch lengths near the gun allow for reduced density of space charge, and thus it is expected that the optimizer will push for long pulses, up to the limits set by rf-focusing induced emittance growth. This is in fact the situation we observe in the dc gun case, whereas the SRF gun case never exceeded laser pulse duration of 10 ps rms. The final bunch duration in all cases is constrained to be less than 3 ps rms, primarily driven by the considerations of limiting induced energy spread from long bunches in the main linac of ERL [19].

IV. RESULTS

A. Final emittance

Results for beam emittance from the dc and SRF gun-based photoinjectors are presented in Fig. 7. Each injector type shows the results for different photocathode MTE values. We note that the SRF gun performs better for larger MTE values, whereas the results are essentially identical for MTE $= 0.025$ eV. In what follows, the MTE $= 0.12$ eV case with 80 pC/bunch is studied in more detail. The laser duration for the dc gun is pushed to the longer limit (30 ps rms) in the optimization while the bunch length is being compressed to 3 ps at the end of the beam line without noticeable emittance degradation. Pulse stacking with birefringent crystals is very effective in generating longer pulses and allows a degree of control of the laser temporal profile [20]. Generating 30 ps rms laser pulses with fast rise and fall times may prove challenging. Therefore, the laser pulse duration was constrained to 10 ps rms in one of the optimizations for the dc gun. The results [Fig. 7(a)] show that the final emittance is not very sensitive on the initial laser pulse duration owing to the presence of rf buncher cavity. In what follows, we compare dc and SRF guns for
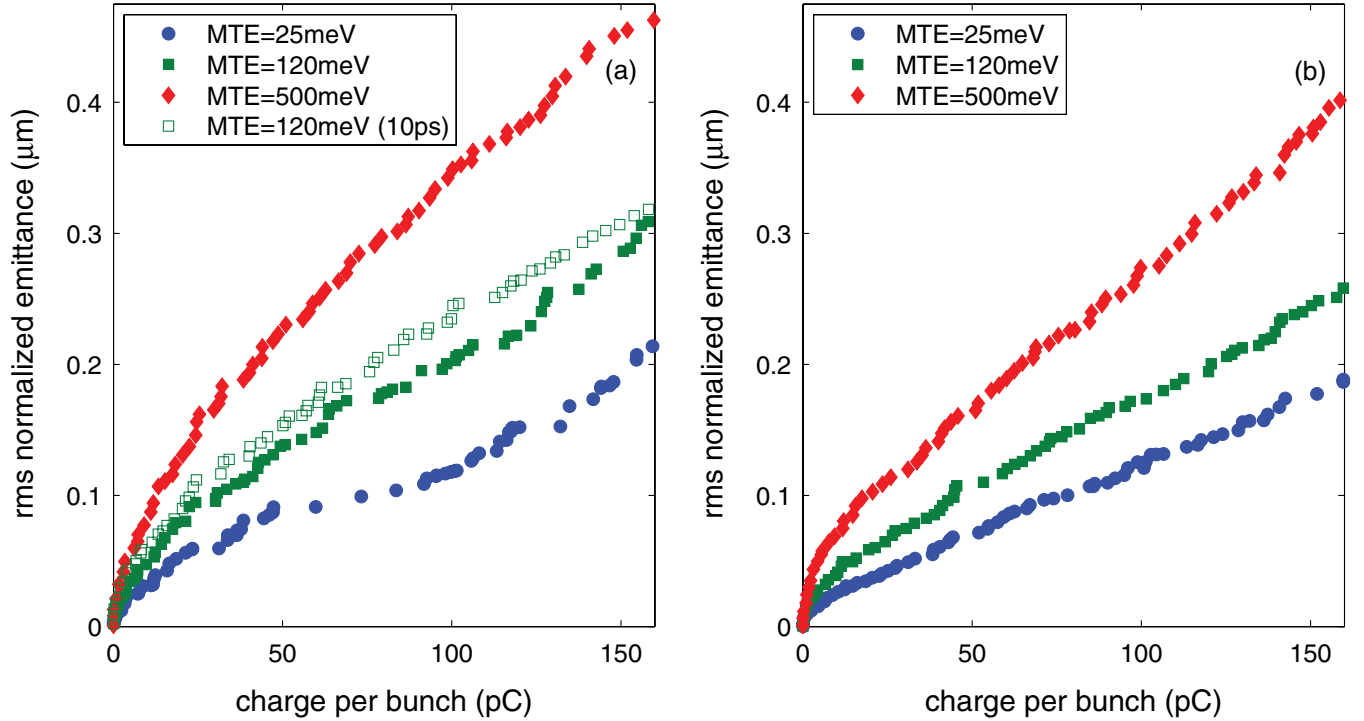
FIG. 7.   Optimized emittance for various bunch charges for (a) dc gun and (b) SRF gun-based photoinjectors.

similar initial laser pulse durations (10 and 9 ps rms, respectively).

The main photoinjector parameters for the two gun cases are given in Table I. The gradients of the first two SRF cavities and their phases are critical parameters and are given in the table. It is seen that large off-crest phase values are chosen for gradual bunch compression (more so for the SRF gun case without a dedicated buncher cavity). The subsequent cavities are less critical and their phases can be chosen more freely, e.g., from considerations of removing correlated energy spread in the bunch.

TABLE I.   Main injector parameters after optimization.

Parameter	dc gun	SRF gun
Charge	80 pC	80 pC
Laser spot size (rms)	0.35 mm	0.21 mm
Laser pulse (rms)	10 ps	9 ps
Thermal emittance (rms)	0.17 μm	0.10 μm
Cathode field ($t = 0$)	5.1 MV/m	16.6 MV/m
Kinetic energy after the gun	0.47 MeV	1.91 MeV
Buncher peak field	1.2 MV/m	$\cdots$
SRF cavities1,2 peak E_z	20, 22 MV/m	11, 6 MV/m
SRF cavities1,2 phase	$-25, -37°$	$-60, -40°$
Solenoid1 peak field	0.038 T	0.094 T
Solenoid2 peak field	0.023 T	$\cdots$
Transverse emittance (rms)	0.21 μm	0.15 μm
Bunch length (rms)	0.89 mm	0.86 mm
Longitudinal emittance (rms)	8.2 mm keV	9.2 mm keV
Kinetic energy	12.4 MeV	10.3 MeV

B. Optimal geometries

Figure 8 shows the optimized field profiles inside the dc and SRF guns. It is interesting to note that the long laser pulse case (30 ps), which has a smaller space charge effect, drives the gun geometry towards a flat cathode electrode ($\alpha \approx 0$) and a gap $g \approx 9$ cm, thereby increasing the photo-cathode field and the voltage. On the other hand, the shorter laser pulse calls for an additional electrostatic focusing and has a cathode angle of $\alpha \approx 10°$ and a shorter gap of $g \approx 6$ cm. The gun voltages are 515 and 475 kV for 30 and 10 ps rms pulse durations, respectively.

The optimized SRF gun geometry for the case presented in Fig. 8(b) has $\alpha = 2.3°$, $g = 4.4$ cm, $r_{pipe} = 0.9$ cm, $r_{cath} = 4$ cm, and no cathode recess. We note that the exit pipe diameter, while always minimized by the optimizer, does not represent a critical parameter and can be enlarged without a significant effect on beam emittance.
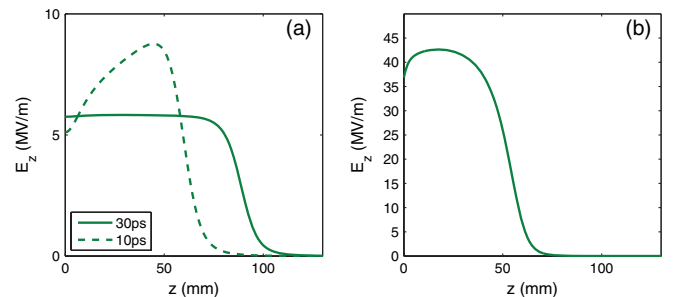

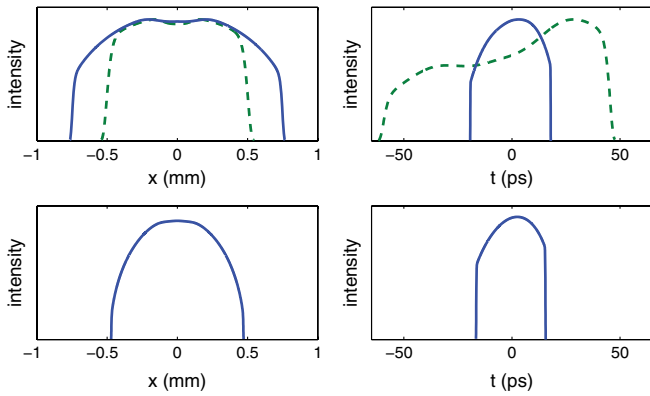FIG. 8.   Field profiles for optimized geometries: (a) dc and (b) SRF guns.

FIG. 9. (Top row) The optimal shape for the dc gun for two different laser pulse lengths, 10 ps (solid) and 30 ps rms (dashed line). (Bottom row) The optimal shape for the SRF gun.

C. Laser shaping

Figure 9 shows the transverse and longitudinal laser profiles selected by the optimizer for 80 pC bunch operation in the two gun cases. All the profiles are normalized to the same peak value and are shown on the same spatial or temporal scale for comparison. It is interesting to note the asymmetric laser profile in the case of dc gun with the longer pulse, which is used to balance off the asymmetric fields arising at the photocathode near the space charge extraction limit [17].

D. Beam envelopes

Figures 10 and 11 show beam envelopes for the two gun cases with 80 pC bunches, along with rms transverse and longitudinal emittances, and beam kinetic energy vs the longitudinal position. For each envelope plot, the transverse projected emittance is evaluated with the effect of
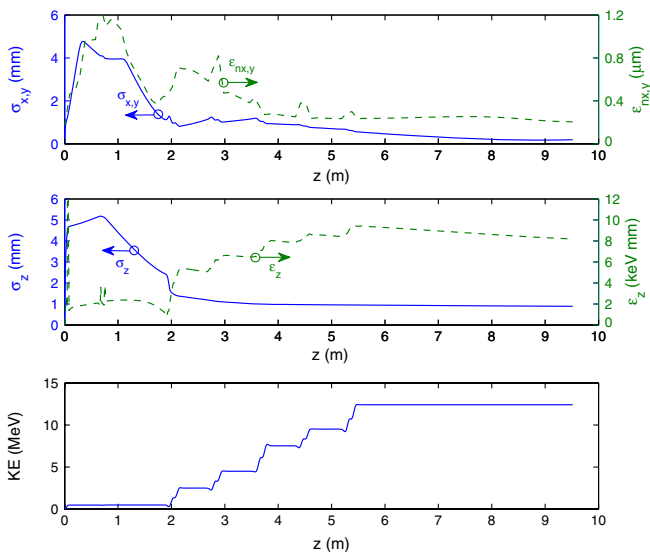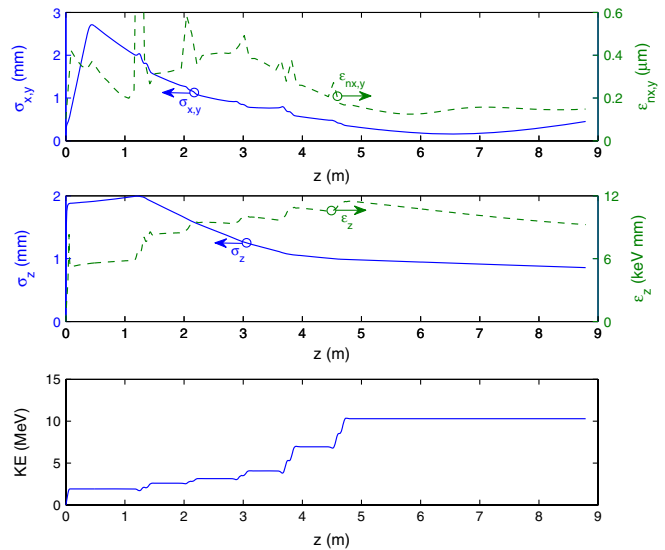

FIG. 11. Beam envelopes for 80 pC (MTE = 120 meV) in the SRF gun photoinjector.

Larmor rotation removed, ridding the curve of spurious emittance spikes. The most salient difference between the two gun types is in ×2 larger beam size at the exit of the dc gun as opposed to the SRF gun, as well as a more dramatic bunch length variation along the longitudinal position in the dc gun photoinjector. The final beam parameters, however, end up being quite comparable between the two gun types. Finally, Fig. 12 shows the final transverse and longitudinal phase spaces near the beam waist ($z = 9.5$ m for the dc and $z = 7$ m for the SRF guns).

E. Performance after the gun

When commissioning either gun type, it is useful to know the expected gun performance just after the gun

FIG. 10. Beam envelopes for 80 pC (MTE = 120 meV) in the dc gun photoinjector. The initial laser pulse is 10 ps rms.
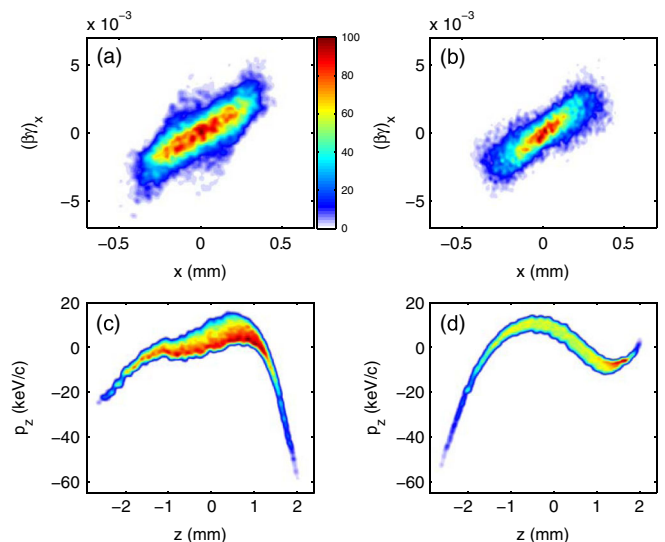

FIG. 12. Examples of the final phase space for 80 pC bunches (MTE = 0.12 eV) for dc [(a),(c)] and SRF [(b),(d)] guns.
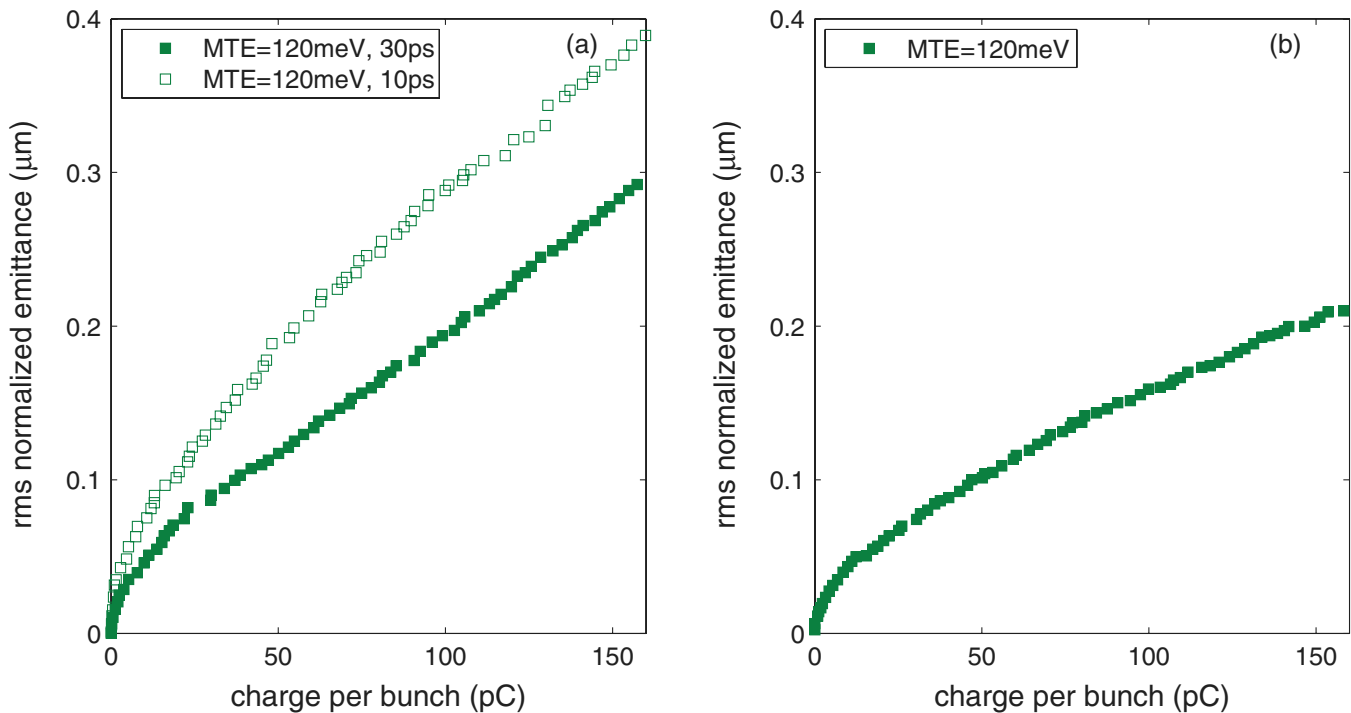
FIG. 13.   Emittance at the end of the shortened beam line for (a) dc and (b) SRF guns.

exit, since that configuration will be most relevant during initial commissioning. Such a study has been performed for the gun geometries shown in Fig. 8. The shorter commissioning beam line consists of either the dc or the SRF gun with a solenoid placed at 0.3 or 0.4 m, respectively (photocathode to the solenoid center) followed by a 1-m drift to emittance measurement diagnostics.

The results summarizing emittance performance for such a short beam line are shown in Fig. 13. Additionally, Fig. 14 shows beam envelope and transverse emittance for 80 pC bunch charge.
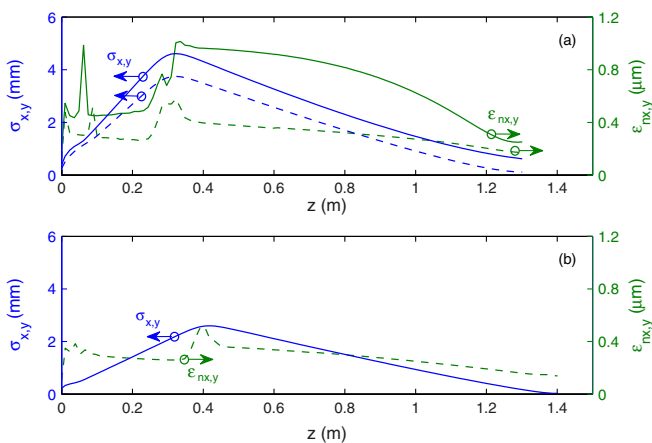

FIG. 14.   Beam envelopes and emittance in the shortened beam line for (a) dc and (b) SRF guns. The dc gun shows two cases: 10 ps (solid) and 30 ps (dashed line) rms initial laser pulse. The photocathode MTE is 120 meV.

It is interesting that the dc gun displays noticeably larger emittance for the 10 ps rms laser pulse when compared to 30 ps, as opposed to only a small change seen in the full ~10 MeV beam line. In this case the larger beam size for the shorter laser pulse causes an increase in the contribution of the solenoid aberrations on final emittance. The question of aberrations and various emittance degrading effects is discussed in detail in the next section.

V. DISCUSSION

Achieving a very low beam emittance requires control of many phase space diluting phenomena, including space charge, optics aberrations, and time-dependent (transverse) rf fields. The fact that the cw operation typically requires accelerating fields that are smaller than what can be accomplished in a pulsed accelerator means that the beam dimensions are necessarily larger with correspondingly increased emittance dilution arising from the sampling of field nonlinearities over a larger spatiotemporal volume.

A. Electric field at the cathode

The electric field at the photocathode sets the lower limit on the laser spot size before the onset of the virtual cathode instability [17]. Together with the photocathode MTE, this decides the smallest achievable emittance. The relevant figure of merit is the electric field during the electron emission, e.g. 5.1 MV/m for the dc and 16.6 MV/m for the SRF guns (see Table I). The cathode's intrinsic emittance scales as $\epsilon_{nxy,\text{th}} \propto \sqrt{1/E_{\text{cath}}}$. In the case of the very
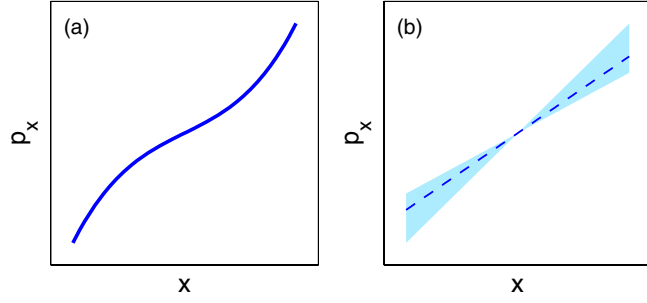
FIG. 15. Examples of projected phase space emittance growth from (a) geometric aberrations and (b) projected (slice) phenomena. The dashed line shows an individual slice either in time (for rf-induced emittance) or in energy (for chromatic aberration).

low MTE (0.025 eV), the final emittance is about 50% due to the intrinsic photocathode emittance and the other 50% from residual emittance degrading effects such as the ones discussed below. The fraction of the cathode intrinsic emittance of the final value becomes larger for higher MTE values.

B. Sources of emittance growth

We differentiate between emittance degrading effects that affect beam slice emittance with those that only increase beam projected emittance, as illustrated in Fig. 15. Aberrations in axially symmetric elements arise from $\propto r^3$ dependencies of transverse fields and are commonly referred to as geometric aberrations. The focal length dependence on beam energy (e.g. in solenoids) or time (in rf cavities) leads to correlated emittance growth which typically does not affect beam slice emittance. This correlated emittance growth can be canceled by other correlated emittance growth mechanisms (rf, space charge, chromatic aberration) that (de)focus beam slices in the opposite direction. We find that the behavior of emittance vs z near the gun in Figs. 10 and 11 can be estimated via semianalytic expressions given below.

1. Solenoid and dc gun aberrations

To evaluate aberrations from magnetic fields in the solenoid, we use the paraxial field expansion to relate the radial component B_r to derivatives of the axial field B_z:

$$B_r = -\frac{r}{2}\frac{\partial B_z}{\partial z} + \frac{r^3}{16}\frac{\partial^3 B_z}{\partial z^3} + \mathcal{O}(r^5), \quad (2)$$

with an analogous expression existing for the electric field. Given the counteracting effect of space charge, we find that the beam size does not change appreciably inside many of the elements. Thus, we can integrate the transverse momentum imparted by the solenoid using a rigid beam approximation (i.e. negligible radial coordinate change inside the element) and write

$$r' = \left(\frac{1}{f}\right)_{sol} r + \alpha r^3. \quad (3)$$

The focal strength has the familiar expression

$$\left(\frac{1}{f}\right)_{sol} = \left(\frac{e}{2mc\beta\gamma}\right)^2 \int B_z^2 dz, \quad (4)$$

whereas the aberration (cubic) coefficient α is given by

$$\alpha = \frac{1}{4}\left(\frac{e}{2mc\beta\gamma}\right)^2 \int \left(\frac{\partial B}{\partial z}\right)^2 dz. \quad (5)$$

The rms (geometric) emittance growth in the Larmor frame can be readily calculated (assuming a zero emittance beam at the entrance):

$$\epsilon_x = \kappa\alpha\sigma_x^4, \quad (6)$$

where $\kappa = \sqrt{8}$, $\sqrt{200/147}$, and $\sqrt{8}/3$ for Gaussian, elliptical, and uniform transverse distributions, respectively. The normalized rms emittance due to this geometric aberration for otherwise identical beams scales inversely with the beam momentum, $\epsilon_{nx} \propto 1/(\beta\gamma)$. When the beam is offset from the solenoid magnetic axis by x_0, the emittance increase squared is given by

$$\epsilon_x^2 = 4\alpha^2\sigma_x^6(5x_0^2 + 2\sigma_x^2) \quad \text{for Gaussian,} \quad (7)$$

$$\epsilon_x^2 = \tfrac{8}{9}\alpha^2\sigma_x^6(9x_0^2 + \sigma_x^2) \quad \text{for elliptical,} \quad (8)$$

$$\epsilon_x^2 = \frac{4}{147}\alpha^2\sigma_x^6(357x_0^2 + 50\sigma_x^2) \quad \text{for uniform.} \quad (9)$$

When $x_0 \ll \sigma_x$ these equations reduce to Eq. (6), whereas for $x_0 \gtrsim \sigma_x$ the emittance increase is given by

$$\epsilon_x \approx \mathcal{K}\alpha\sigma_x^3 x_0. \quad (10)$$

Here $\mathcal{K} = \sqrt{20}$, $\sqrt{68/7}$, and $\sqrt{8}$ for Gaussian, elliptical, and uniform transverse distributions, respectively.

To estimate geometric aberrations from the dc gun, we use numerical integration through the electric field and fit the transverse momentum at the exit of the gun with $p_x = Cx + \alpha_p x^3$, where x is the initial offset on the cathode, C a linear fit coefficient (focusing strength), and α_p the aberration coefficient. The rms normalized emittance in this case is given by an expression analogous to Eq. (6):

$$\epsilon_{nx} = \kappa\sigma_x^4 \frac{\alpha_p}{mc}. \quad (11)$$

For the dc gun, the coefficient α_p/mc evaluates to 0.029 μm/mm^4 resulting in a negligible emittance contribution.

The solenoid has a short focal length, which also leads to strong chromatic effects. Differentiating the focal length, Eq. (4), with respect to beam momentum, we obtain rms normalized emittance increase (in the Larmor frame):

$$\epsilon_{nx} = 2\left(\frac{1}{f}\right)_{\mathrm{sol}} \sigma_x \sqrt{\sigma_x^2 + x_0^2} \frac{\sigma_p}{mc}. \qquad (12)$$

For a longitudinally correlated energy spread, chromatic aberrations do not increase slice emittance, as opposed to geometric aberrations, Eq. (6), and therefore can be readily compensated. This effect is significant for both gun types, although it is larger in the dc gun case due to lower energy and larger beam size.

2. rf focusing

For the rf cavities (SRF gun, rf buncher, and energy booster section), the dominant effect tends to be time-dependent rf focusing. The focusing is a function of cavity gradient, phase, and initial beam kinetic energy. No analytical expression exists for rf focusing in the nonrelativistic regime. We numerically obtain the coefficient of the Taylor expansion for the transverse momentum imparted by the cavity, $\partial^2 p_x / \partial x \partial t$. Overall, the rms normalized emittance contribution is given by

$$\epsilon_{nx} = \frac{1}{mc} \left| \frac{\partial^2 p_x}{\partial x \partial t} \right| \sigma_t \sigma_x \sqrt{\sigma_x^2 + x_0^2}, \qquad (13)$$

x_0 being the offset of the beam with respect to the cavity axis, and σ_t being the rms bunch duration. This effect is significant for the SRF gun, buncher cavity, and the first two SRF cavities.

3. Emittance growth cancellation

We summarize the various emittance contributions greater than $0.1~\mu$m for the cases previously depicted in Figs. 10 and 11 in Table II.

Geometric aberrations are evaluated assuming an elliptical transverse distribution [or uniform in the square brackets]. Where two different values are given in Table II, the values in parentheses were obtained with a rigid beam approximation. A sign has been associated with each correlated emittance growth term, indicating the relative direction of the head-tail rotation of the bunch in phase space between two emittance contributions. The plus sign

TABLE II. Correlated and uncorrelated emittance contributions (rms normalized in μm).

Emittance contribution	dc gun	SRF gun
Thermal emittance	0.17	0.10
SRF gun (rf induced)	$\cdots$	$-0.17(0.11)$
Buncher (rf induced)	0.20	$\cdots$
Solenoid1 (geometric)	0.16[0.13]	<0.1
Solenoid1 (chromatic)	0.8	0.5
Solenoid2 (chromatic)	-0.7	$\cdots$
SRF cavity1	0.7(0.5)	0.3
Final transverse emittance	0.21	0.15

corresponds to $\partial^2 p_x / \partial x \partial z > 0$, or the weaker focusing occurring at the head of the bunch rather than its tail (and vice versa for the minus sign). We see from Figs. 10 and 11 that the scale of emittance increases and reductions is given approximately by the addition of the emittance terms with the appropriate correlation sign as given in Table II. This can be most clearly illustrated for the dc gun case (Fig. 10). The first significant aberration contribution comes from the chromatic effect in the solenoid closest to the gun. At the exit of the dc gun, the space charge forces imprint an energy chirp on the bunch giving a higher energy to the head as opposed to the tail. The resultant chromatic aberration is evaluated to be $0.8~\mu$m, with the head of the bunch experiencing less focusing compared to its tail. A subsequent passage through the buncher further increases the projected emittance by another $0.2~\mu$m while supplying the opposite sign energy chirp to the bunch with the tail now having a larger energy than the head as required for the velocity bunch compression. As a result, the solenoid after the buncher provides an opposite in sign chromatic aberration leading to the projected emittance decrease by about $0.7~\mu$m as seen in Fig. 10. The gradual reduction of the emittance over the scale of meters afterwards, yielding the optimized final emittance, is governed by space charge dynamics and is thus not included in the above estimate formulas. It is evident then that precision control of the 3D laser shaping and beam optics is required to achieve such a high degree of cancellation. However, the analytical expressions given in this section do capture the scale of significant emittance variations near the gun, and therefore should be useful to injector practitioners.

VI. CONCLUSIONS

We have demonstrated a new optimization method, wherein a genetic algorithm is used to dynamically adjust the gun geometry to achieve the lowest beam emittance. A comparison of two technologies, dc and SRF guns, for production of high average current low emittance beams has been performed. Undoubtedly, both approaches will be pursued by the accelerator community in the coming decade. While each approach has its pros and cons, our optimizations show that either is capable of producing similar quality beams of bunch charges up to 154 pC at 1.3 GHz repetition rate corresponding to 200 mA average current. The analysis performed also emphasizes the importance of low mean transverse energy photocathodes.

———————

[1] R. Akre, D. Dowell, P. Emma, J. Frisch, S. Gilevich, G. Hays, P. Hering, R. Iverson, C. Limborg-Deprey, H. Loos, A. Miahnahri, J. Schmerge, J. Turner, J. Welch, W. White, and J. Wu, Phys. Rev. ST Accel. Beams **11**, 030703 (2008).

[2] R. A. Rimmer, in *Proceedings of the 21st Particle Accelerator Conference, Knoxville, 2005* (IEEE, Piscataway, NJ, 2005), pp. 3049–3051.

[3] N. Nishimori, I. Bazarov, B. Dunham, J. Grames, C. Hernandez-Garcia, L. Jones, B. Militsyn, M. Poelker, K. Surles-Law, and M. Yamamoto, in Proceedings of ERL09, Ithaca, New York, USA, 2001, pp. 6–23 [http://www.jacow.org/].

[4] A. Arnold and J. Teichert, Phys. Rev. ST Accel. Beams **14**, 024801 (2011).

[5] I. V. Bazarov and C. K. Sinclair, Phys. Rev. ST Accel. Beams **8**, 034202 (2005).

[6] S. Karkare and I. Bazarov, Appl. Phys. Lett. **98**, 094104 (2011).

[7] I. Bazarov, B. Dunham, C. Gulliford, Y. Li, X. Liu, C. Sinclair, and K. Soong, Phys. Rev. ST Accel. Beams **11**, 100703 (2008).

[8] S. van der Geer and M. de Loos, General Particle Tracer User's Manual, version 2.80, Pulsar Physics (2007).

[9] K. Flottman, ASTRA: a space charge tracking algorithm, DESY (2000).

[10] I. Bazarov and C. Sinclair, Phys. Rev. ST Accel. Beams **8**, 034202 (2005).

[11] S. Bleuler, M. Laumanns, L. Thiele, and E. Zitzler, in *Conference on Evolutionary Multi-Criterion Optimization (EMO 2003)* edited by C. M. Fonseca *et al.* (Springer, Berlin, 2003), Vol. 2632, pp. 494–508.

[12] E. Zitzler, M. Laumanns, and L. Thiele, Computer Engineering and Networks Laboratory (TIK), Technical Report No. 103, ETH Zurich, Switzerland, 2001.

[13] J. Billen and L. Young, POISSON SUPERFISH, Technical Report No. LA-UR-96-1834, Los Alamos, 2000.

[14] B. Aune *et al.*, Phys. Rev. ST Accel. Beams **3**, 092001 (2000).

[15] R. Nagai, R. Hajima, N. Nishimori, T. Muto, M. Yamamoto, Y. Honda, T. Miyajima, H. Iijima, M. Kuriki, M. Kuwahara, S. Okumi, and T. Nakanishi, Rev. Sci. Instrum. **81**, 033304 (2010).

[16] P. G. Slade, The Vacuum Interrupter: Theory, Design, and Application (CRC Press, Boca Raton, FL, 2008).

[17] I. V. Bazarov, B. M. Dunham, and C. K. Sinclair, Phys. Rev. Lett. **102**, 104801 (2009).

[18] I. V. Bazarov, B. M. Dunham, Y. L. Li, X. H. Liu, D. G. Ouzounov, C. K. Sinclair, F. Hannon, and T. Miyajima, J. Appl. Phys. **103**, 054901 (2008).

[19] I. Bazarov and G. Hoffstaetter, in *Proceedings of the 20th Particle Accelerator Conference, Portland, OR, 2003* (IEEE, New York, 2003), pp. 842–844.

[20] I. V. Bazarov, D. G. Ouzounov, B. M. Dunham, S. A. Belomestnykh, Y. L. Li, X. H. Liu, R. E. Meller, J. Sikora, and C. K. Sinclair, Phys. Rev. ST Accel. Beams **11**, 040702 (2008).